Replicative senescence is ATM driven, reversible, and accelerated by hyperactivation of ATM at normoxia

Alexander Stuart and Titia de Lange*
Laboratory for Cell Biology and Genetics
Rockefeller University, New York, USA

Correspondence: Titia de Lange: delange@rockefeller.edu

Abstract

Programmed telomere shortening limits tumorigenesis through the induction of replicative senescence. Here we address three long-standing questions concerning senescence. First, we show that the ATM kinase is solely responsible for the induction of replicative senescence. Senescence was delayed by ATM inhibition (ATMi) or overexpression of TRF2, the shelterin subunit dedicated to ATM repression. In contrast, there was no evidence for ATR signaling contributing to replicative senescence even when ATMi was combined with ATR inhibition. Second, we show ATMi can induce apparently normal cell divisions in a subset of senescent cells, indicating that senescence can be reversed. Third, we show that the extended replicative life span at low (physiological) oxygen is due to diminished ATM activity. At low oxygen, cells show a decreased ATM response to dysfunctional telomeres and genome-wide DSBs compared to 20% oxygen. As this effect could be reversed by NAC, the attenuated response of ATM to critically short telomeres and the resulting extended life span at low oxygen is likely due to ROS-induced formation of cysteine disulfide-bridges that crosslink ATM dimers into a form that is not activated by DSBs. These findings show how primary human cells detect shortened telomeres and reveal the molecular mechanism underlying the telomere tumor suppressor pathway.

Main

Due to the absence of telomerase activity, the telomeres of primary human cells undergo progressive shortening that eventually induces replicative senescence, also referred to as the Hayflick limit (*1-5*). This process represents a cell division counting mechanism that could potentially cull early-stage tumors composed of cells that have reached their Hayflick limit. Consistent with telomere shortening acting as a tumor suppressor pathway, individuals with excessively long telomeres are predisposed to cancer, presumably due to accrual of oncogenic changes before the delayed Hayflick limit arises (*6-8*). In primary fibroblasts, senescence occurs when p53 and p21 are upregulated in response to DNA damage signaling at ~5 critically short telomeres (*9*). In agreement, cells lacking p53 or p21 readily by-pass senescence (*10*, *11*) and dual inhibition of ATM and ATR kinase signaling with kinase-dead alleles can induce S phase entry in a subset of senescent BJ fibroblasts (*12*). However, replicative senescence in BJ fibroblasts may be reversable because they express unusually low levels of p16, which contributes to the long-term maintenance of senescence (*13-15*). To what extent ATM and/or ATR signaling induces replicative senescence and the defect at critically short telomeres that activates the DNA damage response (DDR) remain poorly understood, although it was suggested that critically short telomeres deficient in TRF2 activate ATM signaling (*16*, *17*). It is

also unclear to what extent senescence is reversible and why cells cultured at physiological oxygen levels (e.g., 3%) have a significantly longer replicative life span than those cultured at 20% oxygen (normoxia). Here we provide answers to these questions.

Replicative senescence is caused by ATM, not ATR, signaling

We chose to study replicative senescence in two well-established primary human lung derived fibroblast cell lines, WI38 and MRC5 (*1*, *18*). Senescence was observed at population doubling (PD) 54 when WI38 cells were grown at normoxia (hereafter 20% oxygen) and was delayed until PD62 when cells were cultured at 3% oxygen (physiological oxygen levels) (Fig. 1A). MRC5 fibroblasts underwent senescence around PD71 and PD77 when cultured at 20% and 3% oxygen, respectively (fig. S1A). We applied the following criteria for senescence in WI38 and MRC5 cells: (1) a population doubling limit (PDL) consistent with the literature (*1*, *18*, *19*); (2) fewer than one PD in 10 days; (3) less than 12% of cells showing incorporation of BrdU during a 4-day incubation; (4) more than 30% of cells staining positive for Senescence Associated β-galactosidase (*20-23*) (hereafter β-gal); and (5) less than 40% of cells showing any lamin B1 expression detectable by IF (*21*, *23-26*) (Fig. 1B, C).

In senescent WI38 and MRC5 fibroblasts that were incubated with BrdU for 4 days, there was a significant increase in the BrdU incorporation when the cells were treated with inhibitors to the ATM kinase (ATMi) or its downstream effector Chk2 (Chk2i) (Fig. 1D, E; fig. S1B-D). ATMi and Chk2i induced BrdU incorporation regardless of whether cells had been cultured at 20% or 3% oxygen. In contrast, inhibition of the kinase activity of ATR (ATRi) or Chk1 (Chk1i) did not induce DNA replication in senescent fibroblasts regardless of the oxygen level (Fig. 1D, E; fig. S1B-C). Furthermore, addition of ATR kinase pathways inhibitors in combination with ATMi did not increase the incorporation of BrdU beyond the effect of ATMi alone, whereas a combination of ATMi and Chk2i led to a further increase in BrdU incorporation (fig. S1E, F). Live-cell imaging data presented below (fig. S3) showed no evidence for cell death in cells treated with Chki or ATRi, indicating that the lack of increased BrdU incorporation after incubation with ATR pathway inhibitors is not due to loss of cells that had entered S phase.

Consistent with the finding that ATM is the main kinase that keeps senescent cells from entering S phase, the proliferative life span of WI38 and MRC5 cells was significantly extended when cells were cultured in the presence of ATMi at either low or high oxygen (Fig. 1F; fig. S1G). We note that at higher concentration, ATMi reduced the proliferative life span (fig. S1H), most likely

due to a toxic off-target effect. In cells that had reached senescence after culturing in 3% oxygen in the presence of ATMi, inhibition of the ATR pathway again did not increase the BrdU incorporation (fig. S1I, J). These data indicate that activation of ATM signaling is the main mechanism by which WI38 and MRC5 cells arrest in the cell cycle in response to shortened telomeres at both low and high oxygen.

To further confirm that ATM signaling is primarily responsible for the entry into senescence, we tested whether senescence could be delayed by overexpression of TRF2, the shelterin subunit that represses ATM signaling at functional telomeres (*27*). Indeed, TRF2 overexpression extended the life span of WI38 and MRC5 cells regardless of the oxygen level (Fig. 1G, H; fig. S1K, L), consistent with prior findings in IMR90 cells grown at 20% oxygen (*16*). In contrast, overexpression of POT1 (together with TPP1), which is expected to repress ATR signaling, had no effect and neither did overexpression of Rap1 (Fig. 1G, H; fig. S1K, L). As expected, TRF2-overexpressing cells that had reached senescence did not display an increase in BrdU incorporation after ATMi addition (Fig. 1I; fig. S1M, N). They also did not increase their BrdU incorporation in the presence of ATRi, making it unlikely that these cells underwent senescence due to a deficiency of POT1. Based on these data, we conclude that replicative senescence is initiated by critically short telomeres that induce ATM kinase signaling because they lack sufficient TRF2.

ATM inhibition can induce senescent cells to undergo divisions

Since ATM inhibitors reproducibly induced entry into S phase in a fraction of senescent cells, we examined the fate of these cells using live-cell imaging. Prior to entry into senescence, MRC5 cells were infected with a fluorescent ubiquitination-based cell cycle indicator (FUCCI (*28*)) vector to differentiate between cells in G1, S, and G2 (Fig. 2A). Cells were automatically tracked (*29*) in images captured every 30 min during 44-97 h imaging sessions, and their FUCCI signals were processed to generate tracks in which S/G2 is indicated with green and G1 in grey (Fig. 2A; fig. S2B-G). Cells undergoing mitosis (indicated with yellow) were verified by visual inspection. Approximately half of pre-senescent MRC5 cells (at ~PD66) entered S phase and divided once or twice in a 44.5-h time window (Fig. 2B). Most cell divisions were normal, although there were few (<12%) aberrant cell cycle events which is consistent with cells nearing senescence. As expected, senescent MRC5 cells (imaged at PD78) showed minimal entry into S phase (11% of cells), infrequent normal cell divisions (<4% of all cells), and many cells that entered S phase but did not proceed through a normal cell division (Fig. 2E). This low – but

consistent – frequency of aberrant cell cycle events is consistent with reports of (sub)tetraploid cells in senescent and near-senescent cultures (*30-34*). Inhibition of the kinase activity of ATR or Chk1 had no effect on the cells (fig. S3A, B). In contrast, ATMi not only induced frequent entry into S phase (~25% of cells) but also complete and apparently normal cell divisions after resumption of the cell cycle (Fig. 2D, E). In some cases, two or three consecutive cell divisions were recorded in less than 3 days of imaging (Fig. 2E-G). These data reveal that ATMi can reverse the senescent state. We note that the most of the MRC5 cells used here had been in senescence for around one month. It remains to be seen whether ATMi has the same effect on cells that have been senescent for longer time periods when the Senescence Associated Secretory Pathway (SASP) and its paracrine effects are likely to generate a state that is no longer sensitive to ATMi (*15*, *35*).

Accelerated senescence at 20% oxygen is due to greater ATM response to DSBs

It was proposed that the more rapid senescence at 20% oxygen is partly due to accelerated telomere shortening (*36*, *37*). However, this proposal is not inconsistent the observation that senescence occurs within a few PDs when cells are switched from 3% to 20% oxygen (*38*) (Fig. 3A), or with the finding that cells in low oxygen senesce with slightly shorter average telomere lengths (*36*, *37*, *39*). Furthermore, USTELA and genomic blotting showed that telomeres were not shorter in cells that had undergone senescence at 20% oxygen (Fig. 3B; fig. S4AB, C). In fact, the burden of very short telomeres detected with USTELA appeared significantly higher in cells that had senesced at 3% oxygen (Fig. 3C; fig. S4B, C), indicating that very short telomeres are better tolerated at lower oxygen levels. This tolerance could not be explained by an increase in expression of TRF2 or other shelterin proteins or by diminished expression of ATM, Mre11, or Chk2 at low oxygen (Fig. 3D).

Given the greater tolerance for short telomeres at low oxygen, we tested whether the ATM kinase pathway responded differently to DSBs at low and high oxygen. Remarkably, the formation of γ-H2AX foci in response to zeocin-induced DSBs, a quantifiable proxy for ATM activation, was 2.25-fold and 2.1-fold lower at 3% oxygen in MRC5 and WI38 cells, respectively (Fig. 3E, F). Induction of DSBs with etoposide similarly led to a reduced ATM response at 3% oxygen (Fig S4D). In contrast, there was no effect of oxygen levels on the response to HU, which creates replication stress that activates the ATR kinase (Fig. 3G, F). Similarly, RPE1 cells showed a 2.1-fold lowered in response to DSBs, but not to replication stress, at 3% versus 20% oxygen (Fig. 3G). Comet assays to detect DSBs showed that zeocin induced the same level of DNA damage at 3% and 20% oxygen (Fig. 3H-J). The attenuation of the response of ATM to

DSBs was also observed in a previously characterized RPE1-based system where induction of a dominant negative allele of TRF2 instigates ATM kinase signaling at dysfunctional telomeres (*40*) (Fig. 3K-M). These data suggest that the ATM kinase responds to DSBs and dysfunctional telomeres more robustly at 20% oxygen, explaining why senescence is accelerated at high oxygen.

Since HIF-1α is induced at low oxygen and promotes cell survival (*41-45*), it was prudent to determine whether HIF-1α is responsible for the attenuated response of ATM to DSBs and critically short telomeres at low oxygen. An inducible shRNA that reduced HIF-1α expression detected by western blotting and IF did not affect the induction of γ-H2AX foci in response to zeocin at 3% or 20% oxygen (Fig. 4A-C). As expected, MRC5 cells treated with an inhibitor of HIF-1α translation (HIF-1αi) had a reduced proliferative life span at low oxygen (*41*) (Fig. 4D). However, consistent with ATM being upstream of HIF-1α (*42*, *46*), this reduction in life span was not due to increased ATM signaling since addition of ATMi did not increase the life span of HIF-1α treated cells (Fig. 4D).

It has been shown that low oxygen conditions induce reactive oxygen species (ROS), although the mechanism is not fully understood (*23*, *41*, *44*, *47*, *48*). ROS can induce the formation of ATM dimers that are linked through cysteine disulfide-bridges (*49*, *50*). These covalently-linked ATM kinase dimers are active and target factors involved in ROS tolerance but do not induce a cell cycle checkpoint (*42*, *51-53*). Importantly, ROS-induced ATM kinase dimers cannot be activated by DNA breaks. At DSBs, ATM is activated when MRN bound to DNA ends converts ATM into active monomers that can phosphorylate Chk2 and p53, and this conversion to monomers is not possible when the ATM dimers are held together by disulfide bridges (*51*).

To test whether the ability of ATM to respond to DSBs and critically short telomeres at low oxygen is diminished due to ROS-induced dimerization, we used N-acetyl-cysteine (NAC) which minimizes the formation of disulfide bridges (*49*). At low oxygen, NAC increased the frequency of γ-H2AX foci in response to zeocin (Fig. 4E, F), consistent with preventing the formation of ATM dimers that do not respond to DSBs. Furthermore, NAC reduced the proliferative life span of WI38 and MRC5 cells grown at low oxygen and this effect was in part due to increased ATM activation since treatment with ATMi extended the life span of NAC treated cells (Fig. 4G, H).

These findings are consistent with the observation that resveratrol treatment, which reduces ROS, increases the ATM response to bleomycin induced DSBs (*54*).

Discussion

These data show that replicative senescence occurs when the ATM kinase is activated at critically short telomeres that lack sufficient TRF2 (Fig. 4I). ATM kinase inhibitors extend the life span of primary human cells, as does increased expression of TRF2. We have found no evidence for a role of the ATR kinase in the induction of replicative senescence. We imagine that the critically short telomeres are no longer capable of recruiting sufficient TRF2 to attain the protective t-loop configuration (*55*), allowing MRN to recognize the telomere end and activate ATM. Direct demonstration of a loss of t-loops at critically short telomeres is currently not feasible.

The data also show that inhibition of ATM, but not ATR, induces senescent cells to enter S phase and progress through several, apparently normal, cell divisions, consistent with ATM kinase signaling being primarily responsible for the induction and initial maintenance of senescence. We consider it unlikely that ATM inhibition will induce cell cycle entry of cells that have been senescent for prolonged periods, because their increased SASP may make the senescent state less sensitive to ATMi.

Finally, our data explain why primary human cells have an extended life span at low oxygen, or rather, why cells grown at high oxygen show accelerated senescence. We show that at 20% oxygen, a condition generally used for studying the DNA damage response, the ATM kinase has an increased ability to respond to DSBs. As a result, short telomeres are less tolerated at 20% oxygen and senescence is induced prematurely (Fig. 4I, top). We propose that at low oxygen, ROS-induced ATM dimerization dampens the ATM response to DSBs, leading to greater tolerance of short telomeres and a longer life span (Fig. 4I, bottom).

Methods

Cell culture

MRC5 and WI38 cells were obtained from the ATCC and cultured in EMEM + L-Glutamine (ATCC, 30-2003), 15% fetal bovine serum (FBS, Gibco, 16000-044), 1% penicillin/streptomycin (P/S, Gibco 15140-122). RPE1 ($p53^{-/-}/Rb^{-/-}$ (*56*)), T2p1 (*40*), 293FT, and Phoenix A cells were

grown in DMEM/F12 (1:1) (Gibco, 11330-032), 15% FBS, and 1% P/S. All cells were grown at 37°C, 5% CO_2 in a humidified incubator (Thermo Heracell 240, Cat # 51019560). Low oxygen cells were grown in an incubator maintained at 3% oxygen (Binder, Model CB170, Cat # 9140-0140). Media was replaced every 3-5 days, depending on the proliferation of cells. Time spent outside of 3% oxygen incubator was minimized as much as possible. WI38 and MRC5 cells were trypsinized (Gibco, 25200-056) for ~3-5 min at 37°C, in the oxygen condition-relevant cell incubator. Number of cells was counted each passage (Beckman Coulter Z1 Particle Counter Dual, Cat # 6605699) to calculate population doublings using the standard equation: Log(Total/Seeded)*3.32.

Inhibitors

Inhibitors used were as follows: ATMi/ATMi1, KU-60019 (Selleckchem S1570, DMSO); ATMi2, AZD1390 (Selleckchem S8680, DMSO); ATMi3, KU-55933 (Selleckchem S1092, DMSO); ATRi/ATRi1, AZD6738 (Selleckchem S7693, DMSO); ATRi2, AZ20 (Selleckchem S7050, DMSO); ATRi3, M4344 (Selleckchem S9639, DMSO); Chk2i, BML-277(Selleckchem S8632, DMSO); Chk1i, CHIR-124 (Selleckchem S2683, DMSO). Media solutions were always 0.05% DMSO. Media with compound changed every 3-4 days. For NAC treatment, a 0.5 M solution (filter sterilized) of N-acetyl Cysteine (NAC) (Thermofisher, A15409.14) was used to add NAC at 5 mM to HEPES-NaOH (5 mM, pH 7.5) buffered culture media. NAC media was replaced every 3-4 days. Cells prepared for γ-H2AX IF were incubated with 5 mM NAC for 2 days before DNA damage induction.

BrdU incorporation assay

Approximately 40,000, and 15,500 cells were plated in 35 mm or 24-well microscope-compatible dishes, respectively (Ibidi, 81156 and 82426). After 3 days, media was replaced with media containing 10 μM BrdU (Sigma, B5002) together with relevant inhibitors in DMSO or DMSO alone, all brought to a final equivalent concentration of DMSO (0.05%). Cells were incubated for 4 days, washed with PBS (Corning, 21-040-CV), and fixed in 2% formaldehyde. After two more PBS washes, β-gal staining was performed using CellEvent Senescence Green Detection Kit (Invitrogen, C10851) according to manufacturer instructions. 4N HCl for 10 min was used to denature the DNA in preparation of BrdU staining. After 3 PBS washes, cells were blocked for 1 h using IF blocking buffer (1 mg/mL BSA, 3% Goat Serum, 0.1% Triton-X 100, 1 mM EDTA pH 8.0), followed by 1 h of BrdU-Alexa647 conjugated antibody (Abcam, ab220075) 1:500 in IF blocking buffer combined with Laminb-Coralite594 conjugated antibody (Proteintech, CL594-

66095), 1:250-1:500. Protected from light during and after BrdU/LaminB1 Ab incubation. One PBS wash, incubation in DAPI (0.5 mg/mL) 1:3000 in PBS for five min, one PBS wash. 10-min incubation in 2% formaldehyde, followed by three PBS washes. Fixed samples were then imaged on the CellDiscoverer 7 (Zeiss) at 5X (usually) or 10X (occasionally) magnification, with the following LED settings: DAPI 385 nm 75% gain, 190 ms exposure at 30% intensity; AF647 at 625 nm 50% gain, 1400 ms exposure at 30% intensity; AF488 470 nm 100% gain, 150 ms exposure at 30% intensity; AF594 590 nm 75% gain, 200 ms exposure at 30% intensity. Images were then quantified by co-localization using FIJI/ImageJ. Brightness/contrast settings were adjusted to minimize background fluorescence (as judged by fluorescent signal appearing outside of nuclear bodies) to the same settings for all tested samples in each experiment.

Immunofluorescence

IF for γH2AX foci was performed on cells plated on Poly-L Lysine-coated coverslips (Corning, 354085) three days before drug treatment. NAC (5 mM final) was added at least two days before drug treatment. To induce DNA damage zeocin, etoposide, or HU-containing media was equilibrated in the high or low before addition to the cells (usually 2.5 h). Cells were washed with PBS equilibrated at 3% oxygen for >1.5 h and fixed in 2% formaldehyde in 3% oxygen-equilibrated PBS. Samples fixed for five min at 3% oxygen, followed by 5 min at 20% oxygen. All 20% samples followed the same procedure but with the atmospheric oxygen. Cells then treated as above (BrdU incorporation assay) except with no HCl denaturing. γH2AX antibody (Millipore, 05-636) was diluted 1:2000 in IF blocking buffer. The secondary antibody was used at 1:500-1:1000 dilution (Alexa488, Invitrogen A11070). After the final fixation step, slides were mounted on microscope slides (Fisher, 22042944) with a drop of antifade gold (Invitrogen, P36934) and sealed with nail polish hardener (Sally Hansen). Slides were imaged at 60X on DeltaVision microscope (Applied Precision microscope with Coolsnap QE Photometrics camera and SoftWoRx software). Foci were counted manually using ImageJ/FIJI. HIF-1α IF was performed as above with an anti- HIF-1α antibody (Abcam, ab179483) diluted at 1:500 – 1:1000.

IF-FISH for telomere damage

IF-FISH to measure the TIF response in T2p1 cells was performed as described (*57*). TIFs were imaged at 60X or 100X on Deltavision microscope and scored manually using ImageJ/FIJI.

Western blotting

Western blotting was performed as described (*58*). Cell lysates were prepared with RIPA Lysis buffer with 1X Phos-Stop (Roche, 4906837001) and 1X complete protease inhibitor tablets (Roche, 11836170001). 100 μL RIPA (Thermofisher, 89900) was used for 500,000 cells, after which LDS was added to 1x (from a 4x stock, Thermofisher, NP0007) and βME was added to 350 mM. Samples were boiled for 5 min and loaded into SDS-PAGE gels (Invitrogen, XP04122BOX or NP0322BOX). Western blot membranes were blocked in 5% BSA in TBST (TBS + 0.5% Tween20). Primary antibody incubations done overnight at 4°C or 1 h at room temperature. After 3 washes (3 min each) in TBST, membrane were incubated for 1 h at room temperature, followed by 3 more washes in TBST (3 min each). Blots were developed with chemiluminesnce reagent Supersignal West Pico PLUS (Thermofisher, 34580). Antibodies: TRF2, #647 (*59*); TRF1, #371 (*60*); Rap1, #765 (*58*); TIN2, #864 (*61*); TPP1, #1150 (*58*); POT1, #978 (*62*); POT1, Proteintech 10581-1-AP, Vinculin, CST 13901; GAPDH, Invitrogen MA5-15738; Mre11, CST 4895; Chk2, CST 2662; HIF-1α, Abcam ab179483; ATM, CST 2873**;** γ-tubilin, Sigma GTU88.

Live-cell imaging

Cells were plated in 35 mm or 24-well Live-Cell Microscopy plates (Ibidi 81156 and 82426, respectively) and incubated for 2-3 days. Media was replaced with fresh MEM without phenol-red (Corning, 17-305-CV; supplemented with 1% sodium pyruvate (Sigma, S8636), 1% HEPES, 1% L-glutamine, and 15% FBS) containing drugs (or DMSO) on the day of imaging. Media for cells grown at 3% oxygen was pre-equilibrated at 3% oxygen for 1.5 h. Cells were imaged at 30, 45, or 60 min intervals depending on the experiment on a CellDiscover 7 microscope using ZEN3.6 software (Zeiss). Magnification was 5X or 10X, depending on the experiment. Channel intensities are as follows: PGC at 5% intensity, 6 ms exposure time with 70% intensity; mCherry LED 590nm at 75.2% intensity, 500 ms exposure at 30% intensity; TaYFP 5470 nm at 70.3% intensity, 190 ms exposure at 30% intensity. Imaging conditions: 5% CO2, 37°C, and atmospheric oxygen. Brightness/contrast altered during or after imaging was as required, determined empirically, but consistent within one experiment comparing different conditions. The first 7 h of each movie was deleted because of high background at the beginning of each imaging session.

Lentiviral and retroviral infections.

Lentiviral infections were performed as described (*63*)**.** HEK293FT cells were plated at ~4.5 million cells per 10 cm dish one day before transfection. Calcium phosphate transfection was

used to introduce 15.4 μg of lentiviral construct DNA, 15.4 μg pPAX2, and 10 μg pMD2. 12-18 h after transfection, HEK293FT cell media was changed to that of target infection cells. Cells were left in new media for 24 h, after which the supernatant was filtered through a 0.4 μm filter and polybrene (4 μg/mL) was added before addition to target cells. Media on HEK293FT cells was replaced, allowing for 2-3 more applications of filtered media as required. Lentiviral plasmids: tFucci(CA)2, RIKEN BioResource Center, RDB15446; shHIF-1α, plKO.1-TetON-Puro-Hif1a 0819 (Addgene 118704).

Retroviral infections were performed as described (*63*). Briefly, Phoenix A cells (~4.5-5 million) were plated in 10 cm dishes one day before transfection. Calcium phosphate transfection was used to introduce 20 mg retroviral construct DNA and 0.5 μg of GFP expression plasmid as a control for transfection efficiency. At 12-18 h after transfection, media was changed to that of target cells and infection was performed as above for lentiviral infections. Expression constructs: pLPC-Myc-TRF2 (*64*); pLPC-Myc-TRF2ΔRap1 was generated from pLPC-Myc-TRF2 (*64*); pLPC-FLAG-Rap1 (*65*); pLPC-TPP1-IRES-FLAG-POT1 was generated by Gibson cloning using pLPC-FLAG-POT1 (*62*) and geneblocks (**add company**).

USTELA

USTELA was carried out as previously described (*66*)**.** Briefly, cells were trypsinized, collected (5,000 g, 5 min, 4°C) and flash-frozen as pellets or immediately processed. Genomic DNA (gDNA) was obtained using the MagAttract HMW Kit (Qiagen, 67563). Phenol-Chloroform extraction of gDNA was not compatible with U-STELA in our hands. The gDNA was digested overnight with *Mse*I (60 U, NEB, R0525L) and *Nde*I (60U, NEB, R011S). 20 ng of cut DNA was ligated to the 42-mer and 11-mer as described previously (*66*). After ligation, 1 nM telorette mix and 1 μL 1:10 diluted T4 DNA Ligase was added, alongside T4 Ligase Buffer and ddH20 and incubated overnight at 35°C. The next day, samples were heat-inactivated for 20 min at 65°C and diluted to ~5 pg/mL. PCR was performed with Failsafe PCR 2X Mastermix (Lucigen, FSP995H), Failsafe Enzyme (Lucigen, FS99060), and Tel-tail and Adapter primers in 24 μL final volume. PCR conditions: 68°C 5 mins (1X), 95°C 2 mins(1X), 95°C 15s, 58°C 30s, 72°C 12 mins (26X), 72°C 15 mins (1X). Loading dye was adde and samples were run on a 1% agarose gel. Gels were blotted and hybridized with a TTAGGG repeat probe as described (*63*).

Genomic blots to determine TRF length

Southern blotting to measure the length of telomeric restriction fragments was performed as previously described (*67*).

Comet assay

Comet assays were performed using the CometAssay Kit (Biotechne R&D Systems, 4250-050-K) with modifications to avoid changes in zeocin-induced DSBs during the procedure. Cells were treated with 50 μg/mL zeocin for 2 h. Zeocin containing media used for low oxygen was equilibrated to 3% oxygen. After treatment, cells were harvested with trypsin, spun down, and resuspended to a density of ~200,000 cells/mL in PBS equilibrated at 3% oxygen. 5 μL of diluted cells was added to 45 μL melted agarose, mixed, and spread on comet assay slides. Slides were left at 3% or 20% for 30 min and then for 40 min at 4°C in 20% oxygen. Slides were covered with lysis solution for 25 min at 37ºC in 3% or 20% oxygen, followed by 35 min at room temperature at 20% oxygen. Slides were processed according to the manufacturer's instructions and analyzed using the OpenComet publically-available ImageJ plug-in (*68*) (https://cometbio.org).

Tracking of cell cycle stages in live-cell imaging

Raw data generated from TrackMate was visualized on individual-cell and full-experiment scales using a custom Rscript. Because TrackMate requires a designated channel in which to look for trackable units, we created a new channel by combining the RFP and YFP images. Frames with errors in auto-tracking were manually added or removed within TrackMate. A "background track" was manually generated to control for noise and background in the written code by tracking a space in the imaging field with no cells throughout the video. This track was always the last track made (with the highest TRACK ID in Trackmate) for the Rscript analysis.

The major steps the Rscript takes are as follows (see also Fig. S2B). All conditions are first combined into a single data table, on which the 5th percentile value (maximum value of the bottom 5%) for red (mCherry) and green (mVenus) fluorescence are determined. The 5th percentile serves as a baseline that defines "background," and for both channels, each value above background is converted to a "fluorscore," or its number of standard deviations above the baseline. The fluorscores are then passed through a "smoothing" (local regression analysis) "loess" function to neutralize spurious fluorescence spikes or drops caused by cells entering and exiting focus (Fig. S2B). Three different intensities of smoothing are applied and manually checked, ensuring there is no over-correction leading to flattened fluorescence curves.

Two other modifiable parameters in the form of "general background correction" are applied for mCherry and mVenus (HBRc and HBRv, respectively). HBRc and HBRv are numerical constants (0.5-3) that are applied to the background fluorescence, fluorscore, and z-

score values defined by the “background track”. JPEG image outputs for all individual cell tracks are generated with each output track containing six traces: raw fluorescence, z score, fluorscore, small smoothed fluorscore, medium smoothed fluorscore, and large smoothed fluorscore. The x-axis represents the movie frame from which the graphed value came. Values of mCherry and mVenus are shown as separate red and green lines. HBRc/v altered background values are denoted via horizonal dashed lines (see fig. 2B).

For global analysis, we used the fluorscore values to predict the cell cycle phase of a cell in any given frame by passing the data through two functions. The first defined the cell cycle phase (G1, S, or G2) by comparing mCherry and mVenus fluorscore values to their baseline and to each other. The full list of parameters is available at https://github.com/astu17/Trackmate-FUCCI-Code.git. The second function corrects anomalous, aberrant calls that the first function may have made. Each cell track is mapped on a graph where x is the tracked frame, and y is a different cell track. Each block in a track is colored according to its associated cell cycle phase. Tracks are sorted on the y-axis based on the amount of cell cycle-active frames. The x-axis origin represents the beginning of a given cell track. In all cases, each track was manually checked to confirm the given output. Erroneous outputs were manually corrected. Four visualizations of the data are generated: one based on the raw fluorscore, and one for each level of fluorscore smoothing.

In the final tracks presented, G1 cells are gray and S and G2 cells are presented into a single green color indicating cell cycle activity. Divisions were manually labelled with a yellow bar at the frame of division. High initial background necessitated beginning our tracking ~7 h after imaging started. Some videos had more cells than were quantified, and cells tracked were picked at random. In some cases, cells that remained in G1 were incorporated into total quantification while not being included in the tracking.

Materials

Cell Lines

Cell line	Species	Source/Reference
WI38	*Homo sapiens*	ATCC CCL-75
MRC5	*Homo sapiens*	ATCC CCL-171
TP53$^{-/-}$ RB$^{-/-}$ RPE1	*Homo sapiens*	(*56*)
HEK293FT	*Homo sapiens*	Thermofisher R70007
Phoenix A	*Homo sapiens*	ATCC CRL-3213

Plasmids

Plasmid	Source/Reference
shHIF1a (plKO.1-TetON-Puro-Hif1a 0819)	gift from William Kaelin (Addgene: 118704)
psPAX2	Addgene (12260)
pMD2.G	Addgene (12259)
pLPC-TPP1-IRES-FLAG-POT1	cloned here
pLPC-myc-TRF2ΔRAP1	cloned here
pLPC-myc-TRF2	(*64*)
pLPC-FLAG-RAP1	(*65*)
pLPC-FLAG-POT1	(*62*)
pLPC Vector	Addgene (12540)

Antibodies

Protein	RRID	Antibody
TRF2		#647 (*59*) 1:2000 – 1:4000 in 5% BSA/TBST.

TRF1		#370/371 (*60*), 1:1000 in 5% BSA/TBST
TPP1		#1150 (*58*), 1:1000 in 5% BSA/TBST
POT1		#978 (*62*), 1:1000 in 5% BSA/TBST and guanadine renaturation.
TIN2		TIN2, #86 (*61*), 1:2000 in 5% BSA/TBST
Rap1		Rap1, #765 (*58*), 1:2000 in 5% BSA/TBST
POT1	AB_2284057	Proteintech 10581-1-AP, 1:500 in 5% BSA/TBST
Vinculin	AB_2728768	CST 13901, 1:3000 in 5% BSA/TBST
GAPDH	AB_10977387	Invitrogen MA5-15738, 1:3000 in 5% BSA/TBST
γ-tubulin		Sigma, GTU88, 1:2000 in 5% BSA/TBST
Myc tag	AB_331783	CST 2276, 1:2000 in 5% BSA/TBST
Mre11	AB_2145100	CST 4895, 1:1000
FLAG tag	AB_262044	Sigma F1804, 1:1000 in 5% BSA/TBST
ECL Anti-Rabbit	AB_772206	Cytiva NA934, 1:20000 in 5% BSA/TBST
ECL Anti-Mouse	AB_772210	Cyvita NA931, 1:20000 in 5% BSA/TBST
Chk2	AB_2080793	CST 2662, 1:2000 in 5% BSA/TBST
HIF-1α	AB_2732807	Abcam ab179483, 1:1000 – 1:500 in 5% BSA/TBST
γH2AX	AB_309864	Millipore 05-636, 1:1000 – 1:3000 in 5% BSA/TBST
ATM	AB_2062659	CST 2873, 1:1000 in 5% BSA/TBST
BrdU-Alexa647 conjugated antibody	AB_2832196	Abcam ab220075, 1:250 – 1:500 in IF blocking buffer

Laminb-Coralite594 conjugated antibody	AB_2883510	Proteintech CL594-66095, 1:500 in IF blocking buffer
Anti-rabbit Cy5		Invitrogen A10523, 1:500 - 1:1000 in IF blocking buffer
Anti-mouse Cy5		Invitrogen A10524, 1:500 – 1:1000 in IF blocking buffer
Anti-mouse Cy3		Invitrogen A10521, 1:500 – 1:1000 in IF blocking buffer
Anti-mouse Alexa647		Invitrogen A21236, 1:500 – 1:1000 in IF blocking buffer
Anti-mouse Alexa594		Invitrogen A21201, 1:500 – 1:1000 in IF blocking buffer
Anti-rabbit Alexa488		Invitrogen A11070, 1:500 – 1:1000 in IF blocking buffer

USTELA oligos

Oligo name	Sequence
Tel-tail	5’ - TGC TCC GTG CAT CTG GCA TC - 3’
Adapter	5’ - TGT AGC GTG AAG ACG ACA GAA - 3’
42-mer	5’ - TGT AGC GTG AAG ACG ACA GAA AGG GCG TGG TGC GGA CGC GGG - 3’
11+2-mer	5’ - TAC CCG CGT CCG C - 3’
Telorette #1	5’ - TGC TCC GTG CAT CTG GCA TCC CCT AAC - 3’
Telorette #2	5’ - TGC TCC GTG CAT CTG GCA TCT AAC CCT - 3’
Telorette #3	5’ - TGC TCC GTG CAT CTG GCA TCC CTA ACC - 3’
Telorette #4	5’ - TGC TCC GTG CAT CTG GCA TCC TAA CCC - 3’
Telorette #5	5’ - TGC TCC GTG CAT CTG GCA TCA ACC CTA - 3’
Telorette #6	5’ - TGC TCC GTG CAT CTG GCA TCA CCC TAA - 3’

Drugs/Chemicals

Drug/Chemical	Supplier/Solvent
Zeocin	Gibco 46-0509
Olaparib	Selleckchem S1060, DMSO
N-acetyl Cysteine (NAC)	Thermofisher A15409.14, ddH2O
M4344	Selleckchem S9639, DMSO
KU-60019	Selleckchem S1570, DMSO
KU-55933	Selleckchem S1092, DMSO
KC7F2	Selleckchem S7946, DMSO
HU	Fluka 55291, DMSO
Etoposide	Sigma E-1383, DMSO
Doxycycline	Sigma D9891, ddH2O
CHIR-124	Selleckchem S2683, DMSO
BrdU	Sigma B5002, ddH2O
BML-277	Selleckchem S8632, DMSO
AZD6738	Selleckchem S7693, DMSO
AZD1390	Selleckchem S8680, DMSO
AZ20	Selleckchem S7050, DMSO
CellEvent Senescence Green Detection Kit	Invitrogen, C10851

Acknowledgements

We are deeply grateful to Kaori Takai for performing the western blots shown in panel D of Figure 3. We thank Mike Kastan for advice and Bill Kaelin for discussion and the shHIF-1α plasmid. John Maciejowski and the Rockefeller Bio-imaging Resource Center members Crystina Pygaki and Calos Rico for help with live-cell imaging. Erica Wolin and Jamie Phipps are thanked for help with coding. Agata Smogorzewska, Cayla Broton, and Nicky Blobel are thanked for help with the comet assay. We thank all current and past members of the de Lange lab who provided advice during this project. This work was supported by grants from the NIH to T.d.L. (R35CA210036 and R01AG016642).

Figures and Figure Legends

Figure 1. Stuart and de Lange

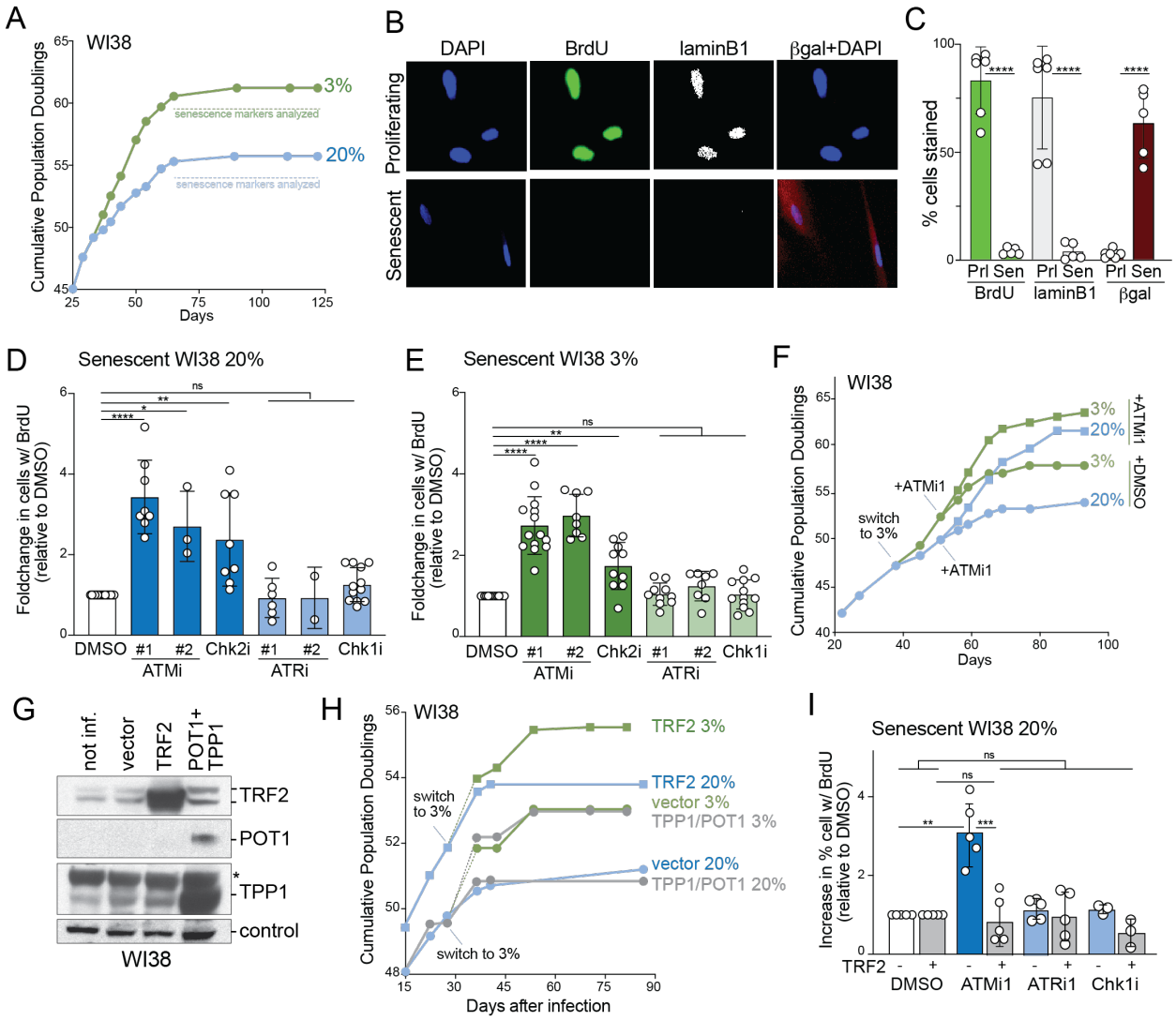

Figure 1. Replicative senescence is due to ATM kinase activation at telomeres lacking sufficient TRF2.

(A) Representative growth curves of WI38 cells in 20% and 3% oxygen. Horizontal lines denote growth stage at which BrdU incorporation and senescent marker were assayed. **(B)** Senescent criteria ascertained by IF for BrdU incorporation for 4 days (2 days for proliferating cells); lamin B1 detected by IF, and an assay for β-gal activity. (**C)** Quantification of the parameter as in (B) of proliferating and senescent cells. >104 cells for each data point. **(D)** Quantification of BrdU incorporation (over 4 days) after treatment of senescent WI38 cells grown at 20% oxygen with

inhibitors of ATM and Chk2 (darker blue) or ATR and Chk1 (lighter blue). Data are given as relative increase compared to DMSO treatment. >100 cells for each data point. **(E)** As in (D) but with cells grown to senescence in 3% oxygen. **(F)** WI38 growth curves with and without long-term ATMi1 treatment at 3% and 20% oxygen. **(G)** Western blots on WI38 cells (PD50) infected with Myc-TRF2 (one infection) or FLAG- TPP1+POT1 (two infections) or with the vector control (2 infections). Antibodies: TRF2, 647; TPP1, 1150; POT1, Proteintech 10581-1-AP. **(H)** Growth curves of WI38 cells as in (G) overexpressing TRF2 or TPP1+POT1. **(I)** Quantification of BrdU incorporation (as in (D)) on senescent WI38 cells overexpressing TRF2 or TPP1+POT1. Statistical significance based on One-way ANOVA for (C-E) and Two-way ANOVA for (I). P-values: **** , < 0.0001; ***, < 0.001; **, < 0.01; * < 0.05. ns, not significant. Inhibitors: ATMi1, 670 nM KU-60019; ATMi2, 1.7 μM AZD1390; Chk2i, 2.5 μM BML-277; ATRi1, 1 μM AZD6738; ATRi2, 100 nM AZ20; Chk1i, 50 nM CHIR-124.

Figure 2. Stuart and de Lange

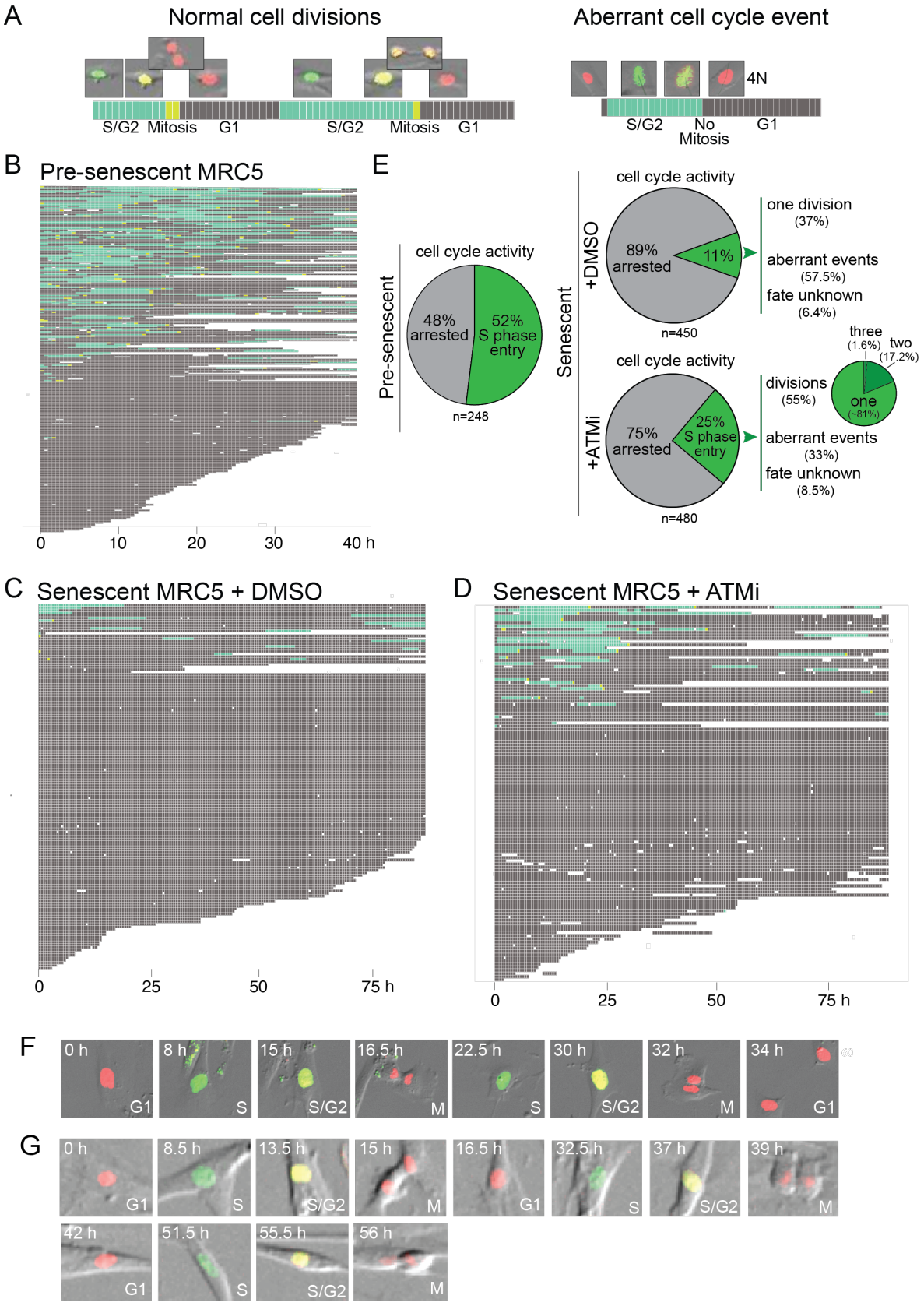

Figure 2. ATM inhibition induces cell divisions in senescent MRC5 cells.
(A) Left: Representative live-cell FUCCI imaging (30 min intervals) track and example images of successful cell divisions in pre-senescent MRC5 cells. Tracks represent cell cycle stages: Green, S/G2; Yellow, mitosis; Grey, G1. Right: Representative track and images of an aberrant cell cycle event in an ATMi-treated senescent cell that by-passes mitosis leading to a 4N G1 cell. **(B)** All recorded cell tracks in pre-senescent MRC5 cells. Rows represent individual tracked cells (n=248). Imaging times indicated below. White: Gaps due to uninterpretable images or cells leaving the field. At least 74% of active cells undergo at least one normal division; 14% had an unknown fate. **(C)** As in (B) but for senescent MRC5 cells (n=144). Representative of 3 replicates. **(D)** As in (B) but for senescent MRC5 cells treated with ATMi (670 nM) (n=122). Representative of 3 replicates. **(E)** Comparison of cell cycle activity in pre-senescent MRC5 cells and senescent MRC5 cells treated with DMSO or ATMi. Data from 3 biological replicates with total numbers of tracked cells indicated. Smaller pie chart (right) representing cells undergoing at least one division. **(F)** and **(G)** Images of cells undergoing multiple divisions in two independent ATMi-treated senescent MRC5 cell cultures.

Figure 3. Stuart and de Lange

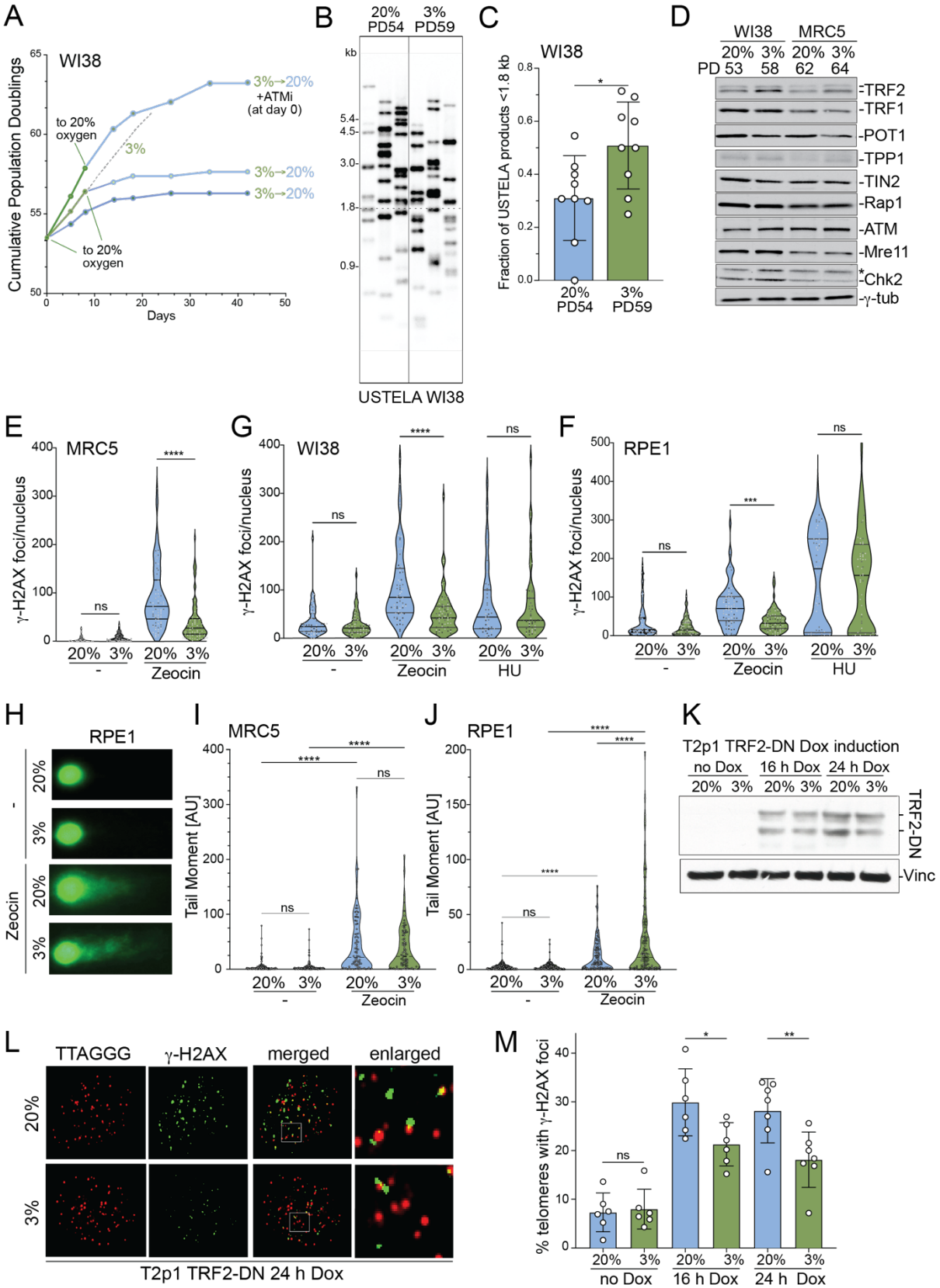

Figure 3. Diminished ATM response to DNA damage response at 3% oxygen

(**A)** Growth curve of WI38 cells grown at 3% oxygen and switched to 20% oxygen as indicated, with or without ATMi1 (670 nM). The switch occurred close at the PD where the cells senesce when in 20% oxygen (see Fig. 1F). Dotted line represents growth trajectory of untreated 3% cells derived from Fig. 1F. **(B)** USTELA products from WI38 cells grown to senescence at high and low oxygen. Three independent PCR reactions for each. **(C)** Quantification of fraction of short USTELA products (less than 1.8 kb) for each PCR reaction as in (B) (n=9). P value (*,<0.05) from unpaired t-test. **(D)** Western blots for the indicated proteins from WI38 and MRC5 cells grown at low or high oxygen. **(E-G)** Quantification of γ-H2AX foci in MRC5, WI38, or RPE1 cells treated zeocin (50 μg/mL, 2.5 h) or HU (2 mM, 2.5 h). n≥3 with 20-25 cells quantified per experiment. **(H)** Representative image of RPE1 comet assay. DNA stained with 1X SYBR Gold. **(I and J)** Quantification of comet assay tail moment in MRC5 and RPE1 cells at the indicated oxygen levels with and without zeocin treatment as in (E) and (F). **(K)** Western blot for TRF2-DN induction 16 and 24 h after dox (1 μg/mL) addition in T2p1 cells at 3% and 20% oxygen. The bottom band is a degradation product. **(L)** IF-FISH detecting TRF2-DN induced γ-H2AX foci at telomeres in T2p1 at 3% and 20% oxygen. **(M)** Quantification of TIFs detected as in (L) (6 independent experiments with 20-30 nuclei quantified in each). All P values determined by Ordinary One-Way ANOVA except for panel (C). P values: **** , < 0.0001; ***, < 0.001; **, < 0.01; * < 0.05. ns, not significant.

Figure 4. Stuart and de Lange

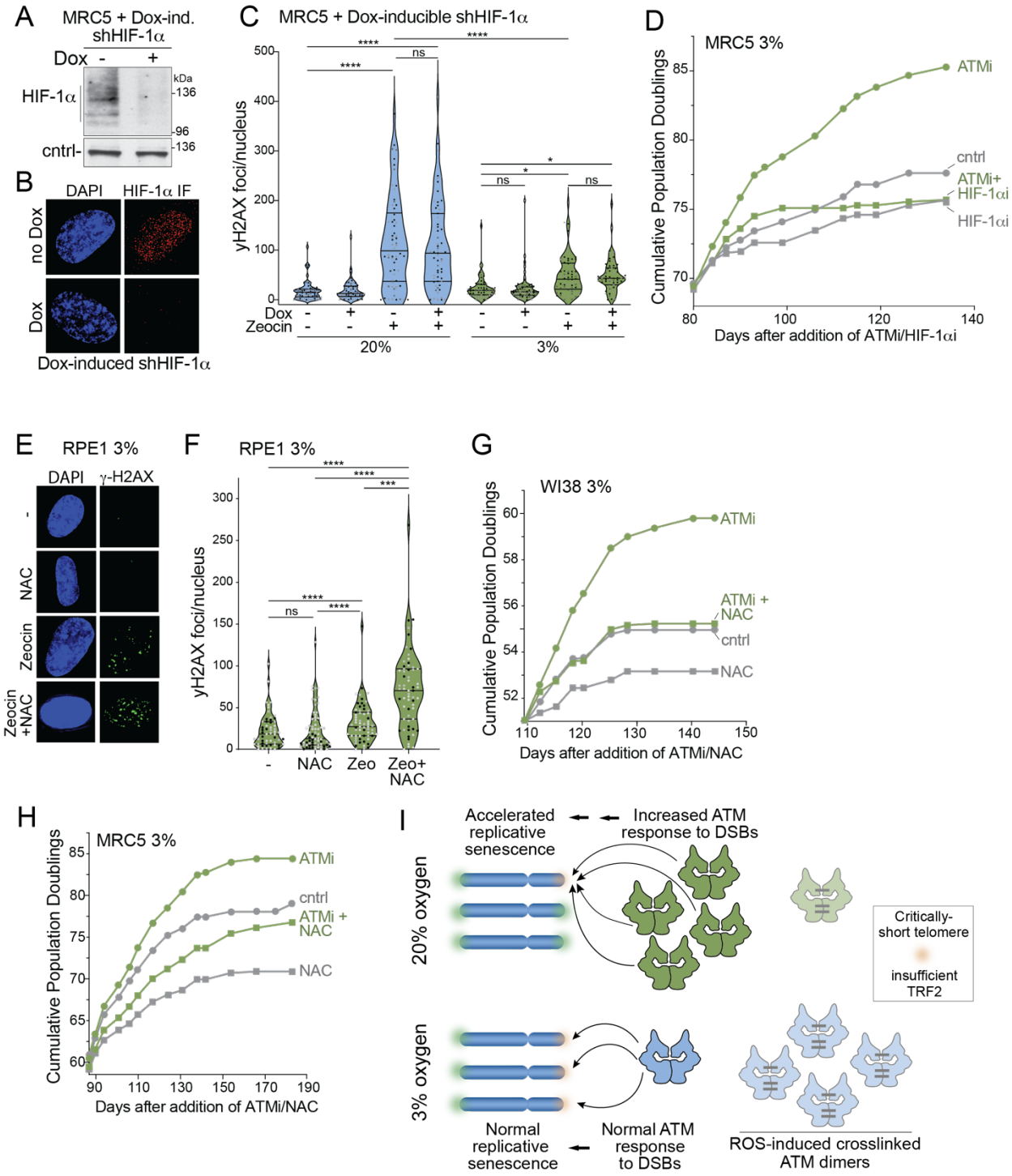

Figure 4. ROS-induced dimerization attenuates the ATM response to DSBs at 3% oxygen. (**A)** Western blot for HIF-1α showing knock down by an inducible shRNA to HIF-1α in MRC5 cells at 3% oxygen. **(B)** IF for HIF-1α in cells as in (A). **(C)** Quantification of the effect of HIF-1α

depletion on zeocin-induced γ-H2AX foci in MRC5 cells at 20% and 3% oxygen. **(D)** Growth curves of MRC5 cells at 3% oxygen, with or without ATMi and/or HIF-1αi. ATMi1, KU-60019, 670 nM; HIF-1αi, KC7F2, 20 μM. **(E)** Representative γ-H2AX IF in RPE1 cells at 3% oxygen after treatment with zeocin (2.5 h, 50 μg/mL), NAC (2 days, 5 mM), or both. **(F)** Quantification of the γ-H2AX foci in RPE1 cells treated as in (E). **(G and H)** Growth curves of WI38 and MRC5 cells at 3% oxygen treated with ATMi1 and NAC as indicated. **(I)** Model of replicative lifespan extension at low oxygen conditions. In physiological conditions (3% oxygen), ROS production induces the formation of disulfide-linked dimeric ATM that is active and induces ROS tolerance but does not respond to DNA damage. The diminished pool of ATM that can respond to DSBs allows cells to tolerate critically short telomeres. At 20% oxygen when there is less ROS-induced ATM dimerization, more ATM can respond to DNA damage. This 'hyperactive' ATM pool responds more robustly to critically-short telomeres, inducing accelerated replicative senescence at normoxia. All P values determined by Ordinary One-Way ANOVA. P values: **** , < 0.0001; ***, < 0.001; **, < 0.01; * < 0.05. ns, not significant.

Supplemental Figures and Figure Legends

fig. S1. Stuart and de Lange

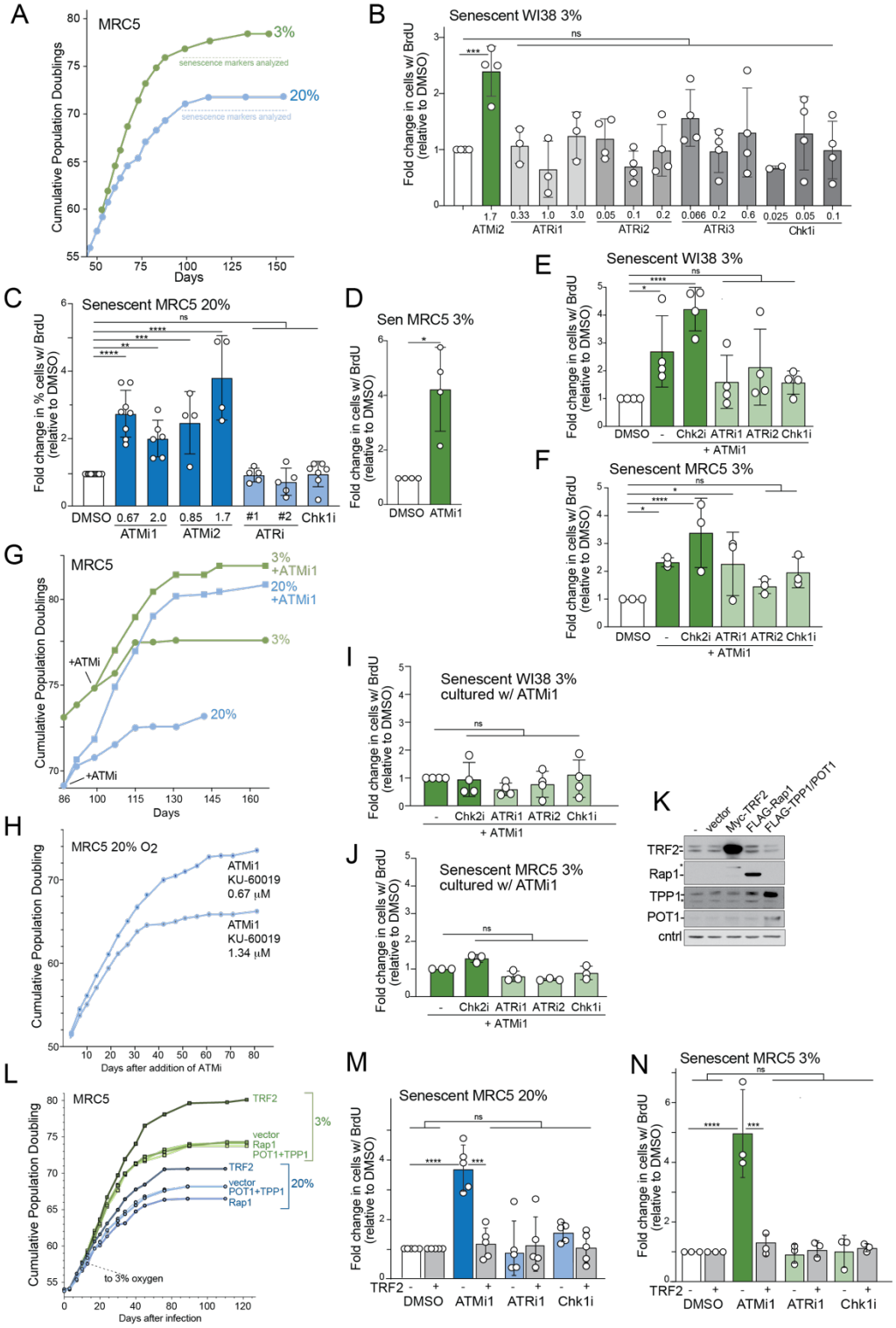

fig. S1. Additional evidence that replicative senescence is due to ATM kinase activation at telomeres lacking sufficient TRF2.

(A) Representative growth curves of MRC5 cells in 20% and 3% oxygen as in Fig. 1A for WI38 cells. **(B)** Additional data on the effect of ATMi, ATRi, and Chk1i on the BrdU incorporation in WI38 cells grown to senescence in 3% oxygen analyzed as in Fig. 1E. **(C)** and **(D)** Effect of the indicated concentrations of ATMi, ATRi, Chk2i, and Chk1i on the BrdU incorporation in MRC5 cells grown to senescence in 20% or 3% oxygen analyzed as in Fig. 1D and E. **(E)** and **(F)** Effect of Chk2i, ATRi, or Chki in combination with ATMi on BrdU incorporation in the indicated cells grown to senescence at 3% oxygen. **(G)** MRC5 growth curves with and without long-term ATMi1 (KU-60019, 670 nM) treatment at 3% and 20% oxygen. **(H)** MRC5 growth curves with two different ATMi1 concentrations (KU-60019, 670 nM and 1.34 μM) at 20% oxygen. **(I)** and **(J)** Effect of combinations of ATMi with Chk2i, ATRi, or Chk1i on the BrdU incorporation of WI38 (I) or MRC5 (J) cells that had grown to senescence in the presence of ATMi. Experiments represent parallel growth, treatment, and quantification with the cells in (E) and (F). **(K)** Western blots for the indicated shelterin subunits in uninfected MRC5 cells or those infected with TRF2, Rap1, TPP1/POT1, or a vector control as indicated. **(L)** Growth curves of MRC5 cells in (K). **(M)** 4-day BrdU incorporation experiment on MRC5 cells grown to senescence and treated in 20% or 3% oxygen, as indicated. Vector-infected or TRF2-overexpressing cells were treated with inhibitors of ATM, ATR or Chk1. Ordinary One-way ANOVA for (B), (C), and (D). Two-way ANOVA for all other panels. P values: **** , < 0.0001; ***, < 0.001; **, < 0.01; * < 0.05. ns, not significant. ATMi, KU-60019; ATMi2, AZD1390; ATRi1. AZD6738; ATRi2, AZ20; ATRi3, M4344; Chk1i, CHIR-124.

fig. S2. Stuart and de Lange

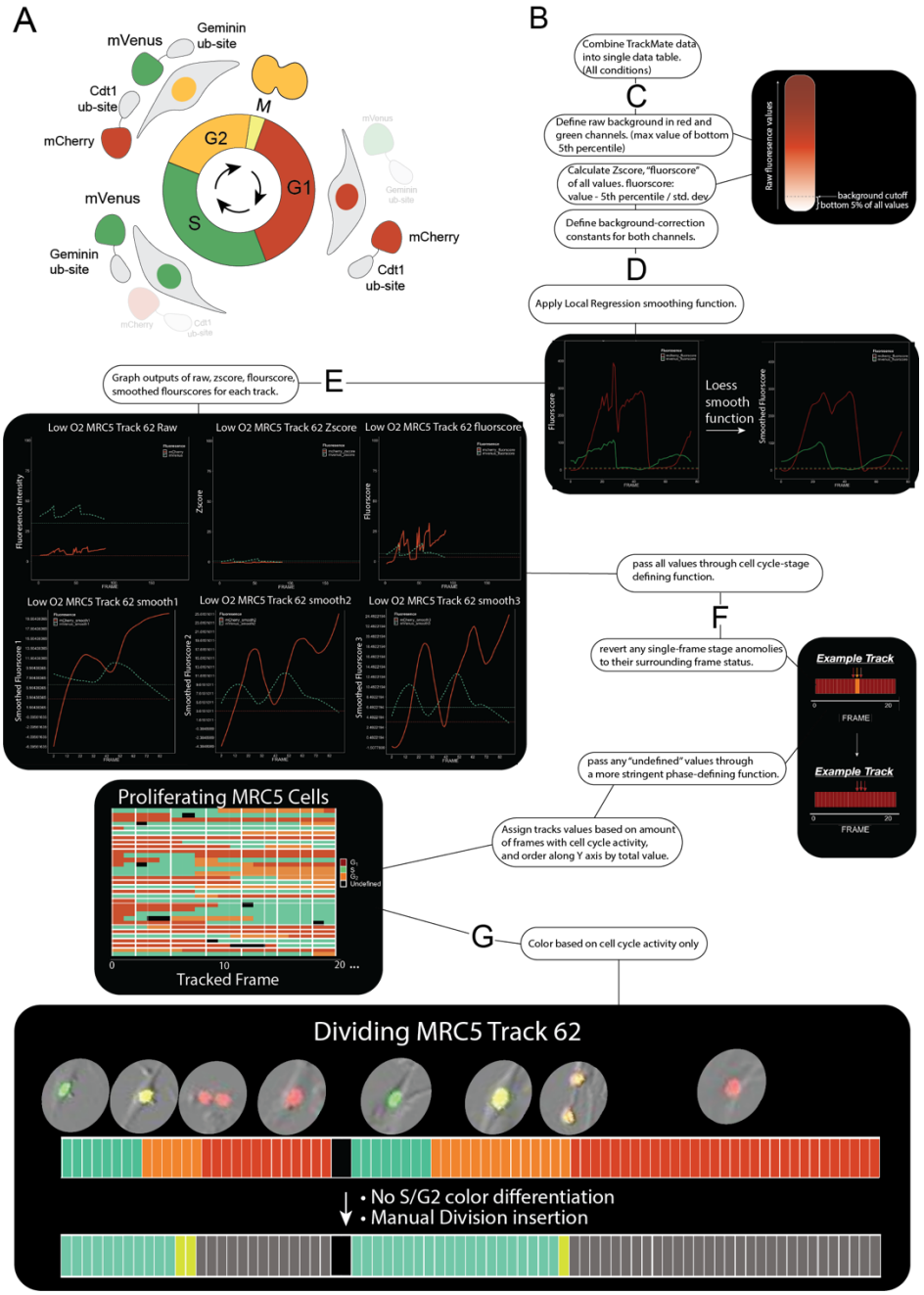

fig. S2. Workflow for analysis of FUCCI live-cell imaging.

(A) Schematic for FUCCI with cell cycle-controlled degrons of Cdt1 and Geminin fused to mCherry and mVenus, respectively. **(B)** Rscript pipeline for largescale Trackmate data analysis. **(C)** Background for both channels defined by the 5th percentile raw value. **(D)** Local regression smoothing function applied to data, which filters out anomalies arising from z-plane changes,

debris, etc. **(E)** Graphical output of data for each individual track. Representative section of larger data set. **(G)** Tracks visualized based on cell cycle activity.

fig. S3. Stuart and de Lange

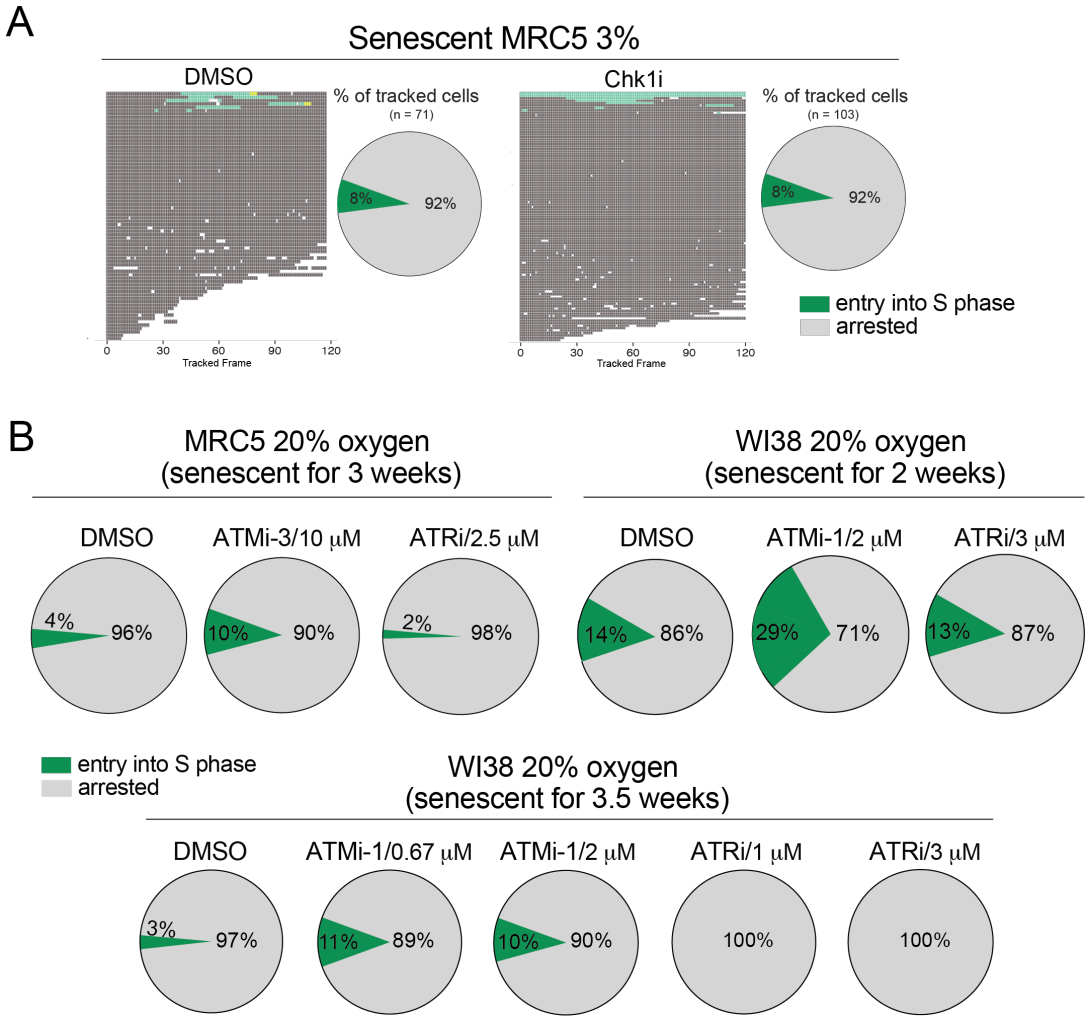

fig. S3. Additional evidence for the reversal of senescence by ATMi, not ATRi.

(A) Imaging tracks and summary of cell cycle activity of MRC5 cells grown to senescence in 3% oxygen treated with Chk1i (CHIR-124, 50 nM) as in Figure 2. Data on control senescent MRC5 cells from Figure 2C and E is shown for comparison. **(B)** Top, left: Cell cycle activity (as in Fig. 2E) of MRC5 cells grown to senescence in 20% oxygen based on tracking 150 cells from a 97-h imaging sessions. ATMi-3, KU-55933 10 μM. Top, right: Cell cycle activity of WI38 cells grown to senescence in 20% oxygen. Experiment conducted after 2 weeks of less than one PD per 10

days. ≥28 cells from a 98-h imaging session. Bottom: Experiment conducted 1.5 weeks later compared to WI38 cells shown above tracking 34 cells in a 94.5-h imaging session.

fig. S4. Stuart and de Lange

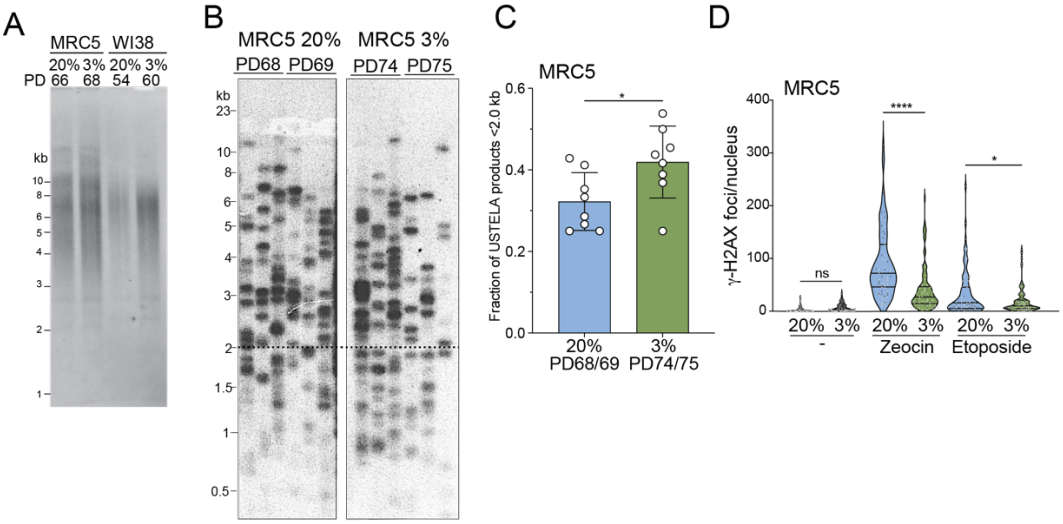

fig. S4. Greater response to DSBs but not telomere length explains early senescence at 20% oxygen.

(A) Genomic blot to detect telomere restriction fragments (TRF) in senescent WI38 and MRC5 cells at high and low oxygen. **(B)** USTELA of paired MRC5 cells grown to senescence at 20% or 3% oxygen as indicated. **(C)** Quantification of USTELAs represented in (B). Fraction of short (less than 2 kb) bands out of total bands in a given USTELA lane from senescent MRC5 cells at low and high oxygen. Each data point represents one PCR reaction. (D) Quantification of γ-H2AX foci in cells treated for 2.5 h with zeocin (50 μg/mL), etoposide (2.5 μM), or HU (2 mM). n≥3 with 20-25 cells per experiment. P values determined by Ordinary One-Way ANOVA except for panel (C) where Unpaired t-test was used. P values: **** , < 0.0001; ***, < 0.001; **, < 0.01; * < 0.05. ns, not significant.

References

1. L. HAYFLICK, THE LIMITED IN VITRO LIFETIME OF HUMAN DIPLOID CELL STRAINS. *Exp Cell Res* **37**, 614-636 (1965).

2. L. HAYFLICK, P. S. MOORHEAD, The serial cultivation of human diploid cell strains. *Exp Cell Res* **25**, 585-621 (1961).

3. A. G. Bodnar, M. Ouellette, M. Frolkis, S. E. Holt, C. P. Chiu, G. B. Morin, C. B. Harley, J. W. Shay, S. Lichtsteiner, W. E. Wright, Extension of life-span by introduction of telomerase into normal human cells. *Science* **279**, 349-352 (1998).

4. H. Vaziri, S. Benchimol, Reconstitution of telomerase activity in normal human cells leads to elongation of telomeres and extended replicative life span. *Curr Biol* **8**, 279-282 (1998).

5. M. T. Hemann, M. A. Strong, L. Y. Hao, C. W. Greider, The shortest telomere, not average telomere length, is critical for cell viability and chromosome stability. *Cell* **107**, 67-77 (2001).

6. I. Schmutz, A. R. Mensenkamp, K. K. Takai, M. Haadsma, L. Spruijt, R. M. de Voer, S. S. Choo, F. K. Lorbeer, E. J. van Grinsven, D. Hockemeyer, M. C. Jongmans, T. de Lange, TINF2 is a haploinsufficient tumor suppressor that limits telomere length. *Elife* **9**, e61235 (2020).

7. Y. Gong, A. J. Stock, Y. Liu, The enigma of excessively long telomeres in cancer: lessons learned from rare human POT1 variants. *Curr Opin Genet Dev* **60**, 48-55 (2020).

8. M. R. Jensen, A. M. Jelsig, A. M. Gerdes, L. R. Hölmich, K. H. Kainu, H. F. Lorentzen, M. H. Hansen, M. Bak, P. A. Johansson, N. K. Hayward, T. Van Overeem Hansen, K. A. W. Wadt, TINF2 is a major susceptibility gene in Danish patients with multiple primary melanoma. *HGG Adv* **4**, 100225 (2023).

9. Z. Kaul, A. J. Cesare, L. I. Huschtscha, A. A. Neumann, R. R. Reddel, Five dysfunctional telomeres predict onset of senescence in human cells. *EMBO Rep* **13**, 52-59 (2011).

10. J. P. Brown, W. Wei, J. M. Sedivy, Bypass of senescence after disruption of p21CIP1/WAF1 gene in normal diploid human fibroblasts. *Science* **277**, 831-834 (1997).

11. J. W. Shay, O. M. Pereira-Smith, W. E. Wright, A role for both RB and p53 in the regulation of human cellular senescence. *Exp Cell Res* **196**, 33-39 (1991).

12. F. d'Adda di Fagagna, P. M. Reaper, L. Clay-Farrace, H. Fiegler, P. Carr, T. Von Zglinicki, G. Saretzki, N. P. Carter, S. P. Jackson, A DNA damage checkpoint response in telomere-initiated senescence. *Nature* **426**, 194-198 (2003).

13. C. M. Beauséjour, A. Krtolica, F. Galimi, M. Narita, S. W. Lowe, P. Yaswen, J. Campisi, Reversal of human cellular senescence: roles of the p53 and p16 pathways. *EMBO J* **22**, 4212-4222 (2003).

14. A. Takahashi, N. Ohtani, K. Yamakoshi, S. Iida, H. Tahara, K. Nakayama, K. I. Nakayama, T. Ide, H. Saya, E. Hara, Mitogenic signalling and the p16INK4a-Rb pathway cooperate to enforce irreversible cellular senescence. *Nat Cell Biol* **8**, 1291-1297 (2006).

15. M. Reimann, S. Lee, C. A. Schmitt, Cellular senescence: Neither irreversible nor reversible. *J Exp Med* **221**, e20232136 (2024).

16. J. Karlseder, A. Smogorzewska, T. de Lange, Senescence induced by altered telomere state, not telomere loss. *Science* **295**, 2446-2449 (2002).

17. U. Herbig, W. A. Jobling, B. P. Chen, D. J. Chen, J. M. Sedivy, Telomere shortening triggers senescence of human cells through a pathway involving ATM, p53, and p21(CIP1), but not p16(INK4a). *Mol Cell* **14**, 501-513 (2004).

18. J. P. Jacobs, C. M. Jones, J. P. Baille, Characteristics of a human diploid cell designated MRC-5. *Nature* **227**, 168-170 (1970).

19. B. P. McSharry, C. J. Jones, J. W. Skinner, D. Kipling, G. W. G. Wilkinson, Human telomerase reverse transcriptase-immortalized MRC-5 and HCA2 human fibroblasts are fully permissive for human cytomegalovirus. *J Gen Virol* **82**, 855-863 (2001).

20. G. P. Dimri, X. Lee, G. Basile, M. Acosta, G. Scott, C. Roskelley, E. E. Medrano, M. Linskens, I. Rubelj, O. Pereira-Smith, A biomarker that identifies senescent human cells in culture and in aging skin in vivo. *Proc Natl Acad Sci U S A* **92**, 9363-9367 (1995).

21. I. Matias, L. P. Diniz, I. V. Damico, A. P. B. Araujo, L. D. S. Neves, G. Vargas, R. E. P. Leite, C. K. Suemoto, R. Nitrini, W. Jacob-Filho, L. T. Grinberg, E. M. Hol, J. Middeldorp, F. C. A. Gomes, Loss of lamin-B1 and defective nuclear morphology are hallmarks of astrocyte senescence in vitro and in the aging human hippocampus. *Aging Cell* **21**, e13521 (2022).

22. M. Sadaie, R. Salama, T. Carroll, K. Tomimatsu, T. Chandra, A. R. Young, M. Narita, P. A. Pérez-Mancera, D. C. Bennett, H. Chong, H. Kimura, M. Narita, Redistribution of the Lamin B1 genomic binding profile affects rearrangement of heterochromatic domains and SAHF formation during senescence. *Genes Dev* **27**, 1800-1808 (2013).

23. T. Shimi, V. Butin-Israeli, S. A. Adam, R. B. Hamanaka, A. E. Goldman, C. A. Lucas, D. K. Shumaker, S. T. Kosak, N. S. Chandel, R. D. Goldman, The role of nuclear lamin B1 in cell proliferation and senescence. *Genes Dev* **25**, 2579-2593 (2011).

24. A. S. Wang, P. F. Ong, A. Chojnowski, C. Clavel, O. Dreesen, Loss of lamin B1 is a biomarker to quantify cellular senescence in photoaged skin. *Sci Rep* **7**, 15678 (2017).

25. A. Freund, R. M. Laberge, M. Demaria, J. Campisi, Lamin B1 loss is a senescence-associated biomarker. *Mol Biol Cell* **23**, 2066-2075 (2012).

26. T. Shimi, R. D. Goldman, in *773*, Eds. Department of Cell and Molecular Biology, Northwestern University Feinberg School of Medicine, Ward Building 11-145 303 E,

Chicago Avenue, Chicago, IL, 60611-3008, USA, takeshi@northwestern.edu., 2014), pp. 415-430.

27. T. de Lange, Shelterin-Mediated Telomere Protection. *Annu Rev Genet* **52**, 223-247 (2018).

28. A. Sakaue-Sawano, M. Yo, N. Komatsu, T. Hiratsuka, T. Kogure, T. Hoshida, N. Goshima, M. Matsuda, H. Miyoshi, A. Miyawaki, Genetically Encoded Tools for Optical Dissection of the Mammalian Cell Cycle. *Mol Cell* **68**, 626-640.e5 (2017).

29. J. Y. Tinevez, N. Perry, J. Schindelin, G. M. Hoopes, G. D. Reynolds, E. Laplantine, S. Y. Bednarek, S. L. Shorte, K. W. Eliceiri, TrackMate: An open and extensible platform for single-particle tracking. *Methods* **115**, 80-90 (2017).

30. P. A. Benn, Specific chromosome aberrations in senescent fibroblast cell lines derived from human embryos. *Am J Hum Genet* **28**, 465-473 (1976).

31. K. H. Walen, Human diploid fibroblast cells in senescence; cycling through polyploidy to mitotic cells. *In Vitro Cell Dev Biol Anim* **42**, 216-224 (2006).

32. K. H. Walen, Bipolar genome reductional division of human near-senescent, polyploid fibroblast cells. *Cancer Genet Cytogenet* **173**, 43-50 (2007).

33. K. H. Walen, Origin of diplochromosomal polyploidy in near-senescent fibroblast cultures: heterochromatin, telomeres and chromosomal instability (CIN). *Cell Biol Int* **31**, 1447-1455 (2007).

34. E. SAKSELA, P. S. MOORHEAD, ANEUPLOIDY IN THE DEGENERATIVE PHASE OF SERIAL CULTIVATION OF HUMAN CELL STRAINS. *Proc Natl Acad Sci U S A* **50**, 390-395 (1963).

35. T. D. Admasu, M. Rae, A. Stolzing, Dissecting primary and secondary senescence to enable new senotherapeutic strategies. *Ageing Res Rev* **70**, 101412 (2021).

36. D. H. Betts, S. D. Perrault, W. A. King, Low oxygen delays fibroblast senescence despite shorter telomeres. *Biogerontology* **9**, 19-31 (2008).

37. N. R. Forsyth, A. P. Evans, J. W. Shay, W. E. Wright, Developmental differences in the immortalization of lung fibroblasts by telomerase. *Aging Cell* **2**, 235-243 (2003).

38. H. Saito, A. T. Hammond, R. E. Moses, The effect of low oxygen tension on the in vitro-replicative life span of human diploid fibroblast cells and their transformed derivatives. *Exp Cell Res* **217**, 272-279 (1995).

39. B. Britt-Compton, F. Wyllie, J. Rowson, R. Capper, R. E Jones, D. M Baird, Telomere dynamics during replicative senescence are not directly modulated by conditions of oxidative stress in IMR90 fibroblast cells. *Biogerontology* **10**, 683-693 (2009).

40. J. Maciejowski, Y. Li, N. Bosco, P. J. Campbell, T. de Lange, Chromothripsis and Kataegis Induced by Telomere Crisis. *Cell* **163**, 1641-1654 (2015).

41. E. L. Bell, T. A. Klimova, J. Eisenbart, P. T. Schumacker, N. S. Chandel, Mitochondrial reactive oxygen species trigger hypoxia-inducible factor-dependent extension of the replicative life span during hypoxia. *Mol Cell Biol* **27**, 5737-5745 (2007).

42. A. H. Rezaeian, C. F. Li, C. Y. Wu, X. Zhang, J. Delacerda, M. J. You, F. Han, Z. Cai, Y. S. Jeong, G. Jin, L. Phan, P. C. Chou, M. H. Lee, M. C. Hung, D. Sarbassov, H. K. Lin, A hypoxia-responsive TRAF6-ATM-H2AX signalling axis promotes HIF1α activation, tumorigenesis and metastasis. *Nat Cell Biol* **19**, 38-51 (2017).

43. M. J. Del Rey, Á. Valín, A. Usategui, C. M. García-Herrero, M. Sánchez-Aragó, J. M. Cuezva, M. Galindo, B. Bravo, J. D. Cañete, F. J. Blanco, G. Criado, J. L. Pablos, Hif-1α Knockdown Reduces Glycolytic Metabolism and Induces Cell Death of Human Synovial Fibroblasts Under Normoxic Conditions. *Sci Rep* **7**, 3644 (2017).

44. D. Kung-Chun Chiu, A. Pui-Wah Tse, C. T. Law, I. Ming-Jing Xu, D. Lee, M. Chen, R. Kit-Ho Lai, V. Wai-Hin Yuen, J. Wing-Sum Cheu, D. Wai-Hung Ho, C. M. Wong, H. Zhang, I.

Oi-Lin Ng, C. Chak-Lui Wong, Hypoxia regulates the mitochondrial activity of hepatocellular carcinoma cells through HIF/HEY1/PINK1 pathway. *Cell Death Dis* **10**, 934 (2019).

45. S. J. Kierans, C. T. Taylor, Regulation of glycolysis by the hypoxia-inducible factor (HIF): implications for cellular physiology. *J Physiol* **599**, 23-37 (2021).

46. H. Cam, J. B. Easton, A. High, P. J. Houghton, mTORC1 signaling under hypoxic conditions is controlled by ATM-dependent phosphorylation of HIF-1α. *Mol Cell* **40**, 509-520 (2010).

47. M. Tafani, L. Sansone, F. Limana, T. Arcangeli, E. De Santis, M. Polese, M. Fini, M. A. Russo, The Interplay of Reactive Oxygen Species, Hypoxia, Inflammation, and Sirtuins in Cancer Initiation and Progression. *Oxid Med Cell Longev* **2016**, 3907147 (2016).

48. G. E. Villalpando-Rodriguez, S. B. Gibson, Reactive Oxygen Species (ROS) Regulates Different Types of Cell Death by Acting as a Rheostat. *Oxid Med Cell Longev* **2021**, 9912436 (2021).

49. Z. Guo, S. Kozlov, M. F. Lavin, M. D. Person, T. T. Paull, ATM activation by oxidative stress. *Science* **330**, 517-521 (2010).

50. A. C. Howes, O. Perisic, R. L. Williams, Structural insights into the activation of ataxia-telangiectasia mutated by oxidative stress. *Sci Adv* **9**, eadi8291 (2023).

51. J. H. Lee, T. T. Paull, Cellular functions of the protein kinase ATM and their relevance to human disease. *Nat Rev Mol Cell Biol* **22**, 796-814 (2021).

52. Z. Bencokova, M. R. Kaufmann, I. M. Pires, P. S. Lecane, A. J. Giaccia, E. M. Hammond, ATM activation and signaling under hypoxic conditions. *Mol Cell Biol* **29**, 526-537 (2009).

53. S. V. Kozlov, A. J. Waardenberg, K. Engholm-Keller, J. W. Arthur, M. E. Graham, M. Lavin, Reactive Oxygen Species (ROS)-Activated ATM-Dependent Phosphorylation of

Cytoplasmic Substrates Identified by Large-Scale Phosphoproteomics Screen. *Mol Cell Proteomics* **15**, 1032-1047 (2016).

54. J. H. Lee, Z. Guo, L. R. Myler, S. Zheng, T. T. Paull, Direct activation of ATM by resveratrol under oxidizing conditions. *PLoS One* **9**, e97969 (2014).

55. Y. Doksani, J. Y. Wu, T. de Lange, X. Zhuang, Super-resolution fluorescence imaging of telomeres reveals TRF2-dependent T-loop formation. *Cell* **155**, 345-356 (2013).

56. Z. Yang, J. Maciejowski, T. de Lange, Nuclear Envelope Rupture Is Enhanced by Loss of p53 or Rb. *Mol Cancer Res* **15**, 1579-1586 (2017).

57. H. Takai, A. Smogorzewska, T. de Lange, DNA damage foci at dysfunctional telomeres. *Curr Biol* **13**, 1549-1556 (2003).

58. K. K. Takai, S. Hooper, S. Blackwood, R. Gandhi, T. de Lange, In vivo stoichiometry of shelterin components. *J Biol Chem* **285**, 1457-1467 (2010).

59. X. D. Zhu, B. Küster, M. Mann, J. H. Petrini, T. de Lange, Cell-cycle-regulated association of RAD50/MRE11/NBS1 with TRF2 and human telomeres. *Nat Genet* **25**, 347-352 (2000).

60. B. van Steensel, T. de Lange, Control of telomere length by the human telomeric protein TRF1. *Nature* **385**, 740-743 (1997).

61. J. Z. Ye, J. R. Donigian, M. van Overbeek, D. Loayza, Y. Luo, A. N. Krutchinsky, B. T. Chait, T. de Lange, TIN2 binds TRF1 and TRF2 simultaneously and stabilizes the TRF2 complex on telomeres. *J Biol Chem* **279**, 47264-47271 (2004).

62. D. Loayza, T. De Lange, POT1 as a terminal transducer of TRF1 telomere length control. *Nature* **423**, 1013-1018 (2003).

63. P. Wu, H. Takai, T. de Lange, Telomeric 3’ overhangs derive from resection by Exo1 and Apollo and fill-in by POT1b-associated CST. *Cell* **150**, 39-52 (2012).

64. A. Smogorzewska, T. de Lange, Different telomere damage signaling pathways in human and mouse cells. *EMBO J* **21**, 4338-4348 (2002).

65. B. Li, S. Oestreich, T. de Lange, Identification of human Rap1: implications for telomere evolution. *Cell* **101**, 471-483 (2000).

66. L. Bendix, P. B. Horn, U. B. Jensen, I. Rubelj, S. Kolvraa, The load of short telomeres, estimated by a new method, Universal STELA, correlates with number of senescent cells. *Aging Cell* **9**, 383-397 (2010).

67. H. Takai, V. Aria, P. Borges, J. T. P. Yeeles, T. de Lange, CST-polymerase α-primase solves a second telomere end-replication problem. *Nature* **627**, 664-670 (2024).

68. B. M. Gyori, G. Venkatachalam, P. S. Thiagarajan, D. Hsu, M. V. Clement, OpenComet: an automated tool for comet assay image analysis. *Redox Biol* **2**, 457-465 (2014).